Doping-induced spin-orbit splitting in Bi-doped ZnO nanowires

Mehmet Aras, Sümeyra Güler-Kılıç,* and Çetin Kılıç†
Department of Physics, Gebze Technical University, 41400 Gebze Kocaeli, Turkey
(Received 24 October 2016; revised manuscript received 4 January 2017; published 5 April 2017)

Our predictions, based on density-functional calculations, reveal that surface doping of ZnO nanowires with Bi leads to a linear-in-k splitting of the conduction-band states, through spin-orbit interaction, due to the lowering of the symmetry in the presence of the dopant. This finding implies that spin polarization of the conduction electrons in Bi-doped ZnO nanowires could be controlled with applied electric (as opposed to magnetic) fields, making them candidate materials for spin-orbitronic applications. Our findings also show that the degree of spin splitting could be tuned by adjusting the dopant concentration. Defect calculations and *ab initio* molecular dynamics simulations indicate that *stable* doping configurations exhibiting the foregoing linear-in-k splitting could be *realized* under reasonable thermodynamic conditions.

DOI: 10.1103/PhysRevB.95.155404

I. INTRODUCTION

The use of quantum wires in spintronic applications is enabled by engineering their inversion asymmetries in the presence of strong spin-orbit (SO) interactions [1–7], which lifts the Kramers degeneracy of the electronic states. Although *doping* could clearly be employed as a means for breaking the inversion symmetry, it remains largely unexplored *if* the spintronic functionalities of a quasi-one-dimensional material could be extended by doping with a heavy element the presence of which usually enhances the SO coupling. The present paper is devoted to exploring the latter, where doping nonmagnetic ZnO nanowires with the heavy element Bi is taken as an exemplar. Our interest in ZnO nanowires stems from the fact that doping them with a variety of elements is practicable, leading to emergent new functionalities. Controlled doping of ZnO nanowires has indeed led to diverse applications in recent years such as photodetectors [8], p-n homojunction rectifiers [9], sensors [10], light-emitting diodes [11], piezoelectric generators [12], field-effect transistors [13], and field emitters [14]. Likewise, doping ZnO nanowires with transition metals [15–17] or rare-earth elements [18,19] makes them candidate building blocks in bottom-up assembly of spintronic devices. To add to the foregoing cases, we will show that the functional properties of ZnO nanowires could further be diversified by doping with Bi, making them candidate materials for spin-orbitronic [20] applications. It should be remarked that Bi-doped ZnO nanowires have not been explored prior to this research as regards the spintronic properties, the electrical properties of which have nevertheless been characterized in experimental [21] and computational [22] studies which agreed that bismuth acts as a *donor* in ZnO nanowires, despite its *acceptor* behavior in ZnO thin films [23] and varistors [24].

We find, via noncollinear density-functional calculations that take into account the SO interaction, that the presence of bismuth as a *substitutional* dopant in a semiconducting ZnO nanowire leads to a linear-in-k spin-orbit splitting of the conduction-band (CB) states. Since the latter facilitates phenomena involving electric-field- and current-induced spin polarization of semiconductor electrons [20,25], our finding implies that Bi-doped ZnO nanowires could be utilized in spintronic applications. Our analysis reveals that the foregoing SO splitting arises from the interaction of the CB electrons (donated by the dopant) with the effective spin-orbit field $\mathbf{B}_{\mathrm{SO}}$ which originates mostly from the inhomogeneous electric potential gradient of the host nanowire. It is interesting to note that this splitting could *not* be attributed to the Dresselhaus [26] and Rashba [27] interactions, the latter being customarily invoked to describe the k-dependent spin splitting in quasi-one-dimensional systems [1–7]. Thus, neither bulk- nor structural-inversion asymmetries [26,27] of the host nanowire alone gives rise to the SO-induced effects explored here, which indeed *cease* to exist in the *absence* of the dopant.

We discuss our findings in detail in Sec. III, following a description of our computational modeling and simulation framework in Sec. II, and present a brief summary in Sec. IV. In the Appendix, we explore the lowering of the symmetry in the presence of the dopant.

II. COMPUTATIONAL MODELING AND SIMULATIONS

We performed geometry optimizations, electronic structure calculations, defect calculations, and finite-temperature *ab initio* molecular dynamics (MD) simulations for a variety of periodic supercells that contain a host (ZnO) nanowire and one or two Bi atoms as dopant and/or adatom, using the Vienna *ab initio* simulation package [28] (VASP) and adopting the rotationally invariant DFT+U approach [29] in combination with the Perdew-Burke-Ernzerhof exchange-correlation functional [30]. We employed the projector augmented wave method [31,32], treating the $2s$ and $2p$, $3d$ and $4s$, and $6s$ and $6p$ states as valence states for oxygen, zinc, and bismuth, respectively. Plane-wave basis sets were used to represent the electronic states, which were determined by imposing a kinetic-energy cutoff of 400 eV. Increasing the latter by 10% resulted in a variation smaller than 0.5% in the SO splitting energies reported in Sec. III. The Hubbard U was applied only to the Zn $3d$ states, the value of which was set to 7.7 eV [22]. The DFT+U approach was preferred over the standard (semilocal) DFT calculations because the inclusion of U improves the underestimation of the d state

*sumeyra@gtu.edu.tr
†cetin_kilic@gtu.edu.tr

binding energies [33], and therefore reduces the spurious *pd* hybridization in the upper valence band of ZnO. In geometry optimizations, ionic relaxations were performed for each atomic structure to minimize the total energy E, until the maximum value of residual forces on atoms was reduced to be smaller than 10^{-2} eV/Å, using the Γ point for sampling the supercell Brillouin zone (BZ). Note that the BZ sampling is virtually achieved through *zone folding* since we in practice use supercells made of n unit cells, as described in the next paragraph, with $n > 4$. To obtain an error bar for E owing to the BZ sampling, we performed a number of test calculations using the primitive unit cell of a host nanowire and increasing the number of **k** points from 4 to 11, which showed a variation in the energy (per ZnO unit) smaller than 0.2 meV. In electronic structure calculations, spin-orbit coupling was taken into account by utilizing the noncollinear mode of VASP [34,35]. A convergence criterion for the electronic self-consistency was set up to 10^{-6} eV (10^{-8} eV) in geometry optimizations (electronic structure calculations). *Ab initio* MD simulations were performed at temperature 600 K with the aid of a Nosé-Hoover thermostat [36], integrating the equations of motion via the Verlet algorithm with a time step of 1 fs.

We considered a variety of atomic configurations within the supercell approach, including the ZnO nanowire with (i) the Bi dopant substituting Zn at a surface site, denoted as $[(\mathrm{ZnO})_N]_n$:$\mathrm{Bi_{Zn}}$; (ii) the Bi adatom, denoted as $[(\mathrm{ZnO})_N]_n$ + Bi; and (iii) the substitutional Bi dopant together with a Bi adatom, denoted as $[(\mathrm{ZnO})_N]_n$ + Bi:$\mathrm{Bi_{Zn}}$. The primitive unit cell for a host nanowire, which contains $(\mathrm{ZnO})_N$, is cut from bulk ZnO in wurtzite structure in such a way that the wire axis coincides with the [0001] direction of wurtzite, and therefore has a hexagonal cross section. A host nanowire $[(\mathrm{ZnO})_N]_n$ is constructed by combining n consecutive unit cells; the supercell length L along the wire axis is given by $L = nc$ where c denotes the length of periodicity along the wire axis. The symmetries of the host nanowires employed in this paper are described by the $R70\,(p6_3mc)$ rod group [37], which means that the undoped $[(\mathrm{ZnO})_N]_n$ nanowire has the same ($\mathrm{C_{6v}}$) point group as bulk (wurtzite) ZnO. The incorporation of the Bi dopant and/or adatom eliminates these symmetries since *no* symmetry elements are present in $[(\mathrm{ZnO})_N]_n$:$\mathrm{Bi_{Zn}}$, $[(\mathrm{ZnO})_N]_n$ + Bi, and $[(\mathrm{ZnO})_N]_n$ + Bi:$\mathrm{Bi_{Zn}}$.

As for the adatom configurations, we computed the adsorption energy $E_{\mathrm{ad}} = E(\text{nanowire + Bi}) - E(\text{nanowire}) - E(\text{Bi})$, where $E(\text{Bi})$ denotes the energy of the Bi atom, and determined the *lowest-energy* adatom configuration. As for the doping configurations, we computed the formation energy as a function of the bismuth chemical potential μ_{Bi} under Zn-*rich* and Zn-*poor* conditions, assuming a chemical equilibrium between the doped nanowire and the reservoirs of its constituent atoms. The formation energy is given by $\Delta H_{\mathrm{f}} = [E(\text{nanowire} + m\ \text{Bi}) - E(\text{nanowire}) + E(\text{Zn}) - mE(\text{Bi})] + \mu_{\mathrm{Zn}} - m\mu_{\mathrm{Bi}}$, where m denotes the number of Bi atoms transferred from the bismuth reservoir to the doped nanowire, i.e., $m = 1$ for $[(\mathrm{ZnO})_{24}]_5$:$\mathrm{Bi_{Zn}}$ and $m = 2$ for $[(\mathrm{ZnO})_{24}]_5$ + Bi:$\mathrm{Bi_{Zn}}$. Here $E(\text{Zn})$ denotes the energy per atom of bulk Zn metal, which is set as the zero of the zinc chemical potential μ_{Zn}. Zn-*rich* and Zn-*poor* conditions correspond, respectively, to $\mu_{\mathrm{Zn}} = 0$ and ΔH_N, where ΔH_N denotes the *heat of formation* (per formula unit) of the nanowire made of N Zn-O pairs, due to the chemical equilibrium between the nanowire and the reservoirs of its constituent atoms. Note that the latter sets the range of values for the oxygen chemical potential μ_{O} as well, since $\mu_{\mathrm{Zn}} + \mu_{\mathrm{O}} = \Delta H_N$.

III. RESULTS AND DISCUSSION

For the optimized atomic structures displayed in Figs. 1(a) and 1(b), viz., $[(\mathrm{ZnO})_{24}]_5$:$\mathrm{Bi_{Zn}}$ and $[(\mathrm{ZnO})_{24}]_5$ + Bi:$\mathrm{Bi_{Zn}}$, the SO-split conduction bands are shown in Figs. 1(c) and 1(d), respectively. It is seen that the dispersion of these bands is *accurately* described by the solid curves (in blue and red) that represent fits in the form

$$\epsilon_{\pm}(k) = \frac{\hbar^2}{2m^*}k^2 \pm \alpha k, \tag{1}$$

which resembles the Bychkov-Rashba expression [27]. The values for the effective mass m^* and the linear coefficient α are given in Table I where the expectation values $\langle \mathbf{m} \rangle_{\pm}$ of the magnetization density $\mathbf{m}(\mathbf{r})$ corresponding to the $\epsilon_{\pm}$ bands are also given. Although these α values appear to be small compared to the values of the Rashba parameter α_{R} in "giant" Rashba systems such as Pt-Si nanowires [7], it should be remarked that the SO splitting here is obtained by adding a *single* heavy atom to a *light* oxide, corresponding to a low (i.e., one Bi atom per 120 Zn-O pairs) concentration. This is appealing because enhancing spin-orbit coupling is usually accomplished by using significant amounts of heavy elements. The α values in Table I are indeed of the same magnitude as the α_{R} values in III-V heterostructures [38], making us expect Bi-doped ZnO nanowires find use in spintronic devices. The linear k dependence of the band energies $\epsilon_{\pm}$ in the vicinity of the conduction-band minimum (CBM) is further confirmed by plotting the splitting energy $\Delta\epsilon = \epsilon_+ - \epsilon_-$ with respect to the wave vector k in Figs. 1(e) and 1(f). The contribution from Bi to the states of the bands in Fig. 1(c) [Fig. 1(d)] is in the range of 3–4% [6–7%], cf. Fig. S1 (see Ref. [39]), showing that these bands are predominantly derived from the respective conduction bands of the host (ZnO) nanowire. Hence the states of the SO-split bands have more of the character of *extended* states that facilitate (spin-polarized) electrical conduction.

Consider, for the purpose of interpretation, a Kramers doublet with two-component spinor wave functions $\psi^-_{\mathbf{k}}(\mathbf{r}) = \psi_{\mathbf{k}}(\mathbf{r})\begin{bmatrix}\cos\frac{\theta}{2}e^{-i\frac{\phi}{2}}\\ \sin\frac{\theta}{2}e^{i\frac{\phi}{2}}\end{bmatrix}$ and $\psi^+_{\mathbf{k}}(\mathbf{r}) = \psi^*_{\mathbf{k}}(\mathbf{r})\begin{bmatrix}-\sin\frac{\theta}{2}e^{-i\frac{\phi}{2}}\\ \cos\frac{\theta}{2}e^{i\frac{\phi}{2}}\end{bmatrix}$ where $\psi_{\mathbf{k}}(\mathbf{r}) = e^{i\mathbf{k}\cdot\mathbf{r}}u_{\mathbf{k}}(\mathbf{r})$ denotes the wave function of the respective Bloch state in the absence of the SO interaction. The expectation value of the SO interaction operator [40] with $\psi^-_{\mathbf{k}}(\mathbf{r})$ can be expressed as

$$\langle \psi^-_{\mathbf{k}} | H_{\mathrm{SO}} | \psi^-_{\mathbf{k}} \rangle = -\langle \mathbf{m} \rangle_- \cdot \langle \mathbf{B}_{\mathrm{SO}}(\mathbf{k}) \rangle, \tag{2}$$

where $\langle \mathbf{B}_{\mathrm{SO}}(\mathbf{k}) \rangle = \int \psi^*_{\mathbf{k}}(\mathbf{r})\mathbf{B}_{\mathrm{SO}}\psi_{\mathbf{k}}(\mathbf{r})d^3r$ is the $\mathbf{k}$-dependent matrix element of the operator $\mathbf{B}_{\mathrm{SO}} = (-\vec{\nabla}V \times \mathbf{p})/2emc^2$ (in the nonrelativistic limit). A similar equation follows for $\langle \psi^+_{\mathbf{k}} | H_{\mathrm{SO}} | \psi^+_{\mathbf{k}} \rangle$, but for our purpose it suffices to focus on $\langle \psi^-_{\mathbf{k}} | H_{\mathrm{SO}} | \psi^-_{\mathbf{k}} \rangle$. According to Eq. (2), a linear-in-k SO splitting as in Eq. (1) occurs *only if* (i) $\langle \mathbf{m} \rangle_-$ is nonzero and (ii) $\langle \mathbf{B}_{\mathrm{SO}}(\mathbf{k}) \rangle$ has nonzero components in the direction parallel

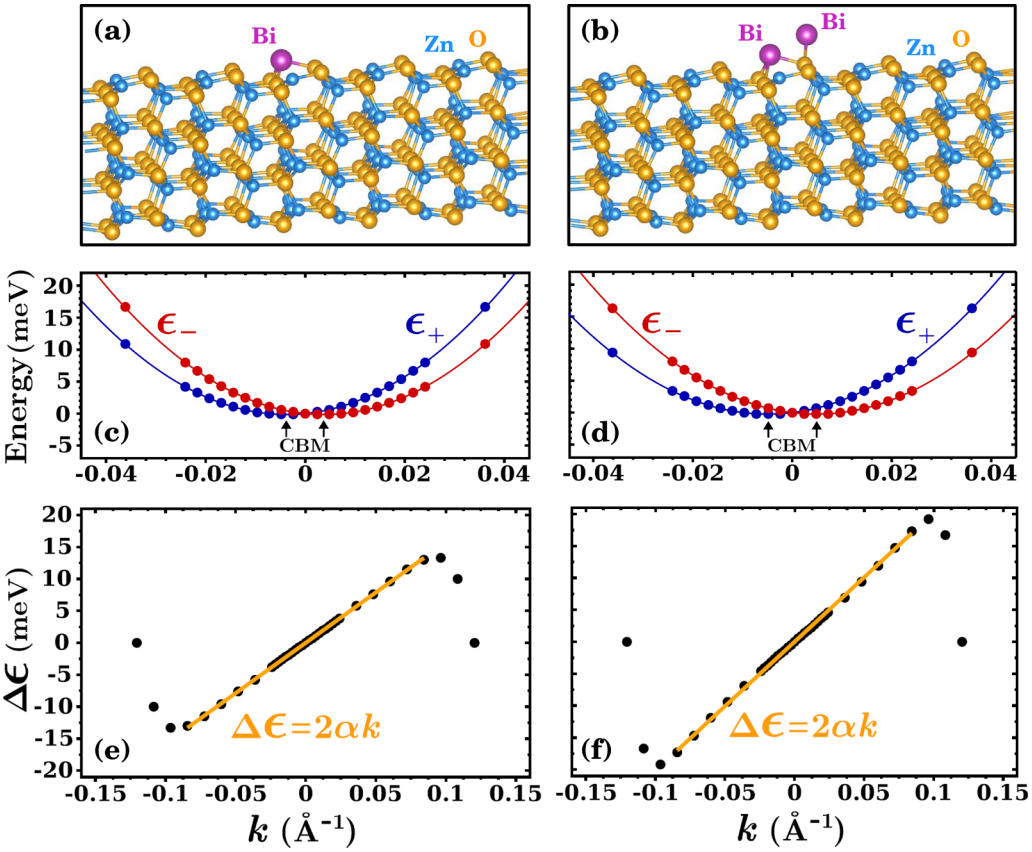

FIG. 1. Optimized atomic structures for (a) $[(ZnO)_{24}]_5$:Bi_{Zn} and (b) $[(ZnO)_{24}]_5 + Bi$:Bi_{Zn}. (c, d) SO-split conduction bands for structures in (a) and (b), respectively. (e, f) Plots showing the variation of the splitting energy $\Delta\epsilon$ with the wave vector k.

to $\langle\mathbf{m}\rangle_-$. The condition (i) is satisfied for $[(ZnO)_{24}]_5$:Bi_{Zn} and $[(ZnO)_{24}]_5 + Bi$:Bi_{Zn} as indicated by the $\langle\mathbf{m}\rangle_\pm$ values given in Table I. In other words, the Bi incorporation leads to *magnetization* of the two lowest CB states although the total magnetic moment $\mathbf{M} = \int \mathbf{m}(\mathbf{r})d^3r$ is *zero* for both $[(ZnO)_{24}]_5$:Bi_{Zn} and $[(ZnO)_{24}]_5 + Bi$:Bi_{Zn}. It remains to be seen if the condition (ii) is also satisfied. It is convenient to use the uvw coordinate system depicted in Figs. 2(a) and 2(b) where $\hat{\mathbf{w}}$ denotes the unit vector in the direction of $\langle\mathbf{m}\rangle_-$. Because of the dot product in Eq. (2), we are interested only in the w component of $\langle\mathbf{B}_{SO}(\mathbf{k})\rangle$ that is perpendicular to the uv plane [cf. Fig. 2(b)]. The latter, i.e., $\langle\mathbf{B}_{SO}(\mathbf{k})\rangle \cdot \hat{\mathbf{w}}$, involves $\partial V/\partial u$ and $\partial V/\partial v$, and does *not* have any term with $\partial V/\partial w$ owing to the cross product in the definition of $\mathbf{B}_{SO}$. In this line of reasoning, the origin of the SO splitting of the bands of $[(ZnO)_{24}]_5$:Bi_{Zn}, cf. Fig. 1(c), is sought by plotting the potential gradient ∇V on the uv plane in Fig. 3(a) where a colored contour plot of the state charge density $|\psi_{CBM}|^2$ is superimposed. Respective plots for the undoped nanowire $[(ZnO)_{24}]_5$ are given in Fig. 3(b) for comparison. The arrows in Figs. 3(a) and 3(b) show the spatial inhomogeneity and asymmetry in the $\partial V/\partial u$ and $\partial V/\partial v$ components of the potential gradient, which gives rise to the effective field $\mathbf{B}_{SO}$, and thus implies the satisfaction of the aforementioned condition (ii). The *centrosymmetric* pattern of arrows around the Bi atom in Fig. 3(a) should be noticed, indicating that the Bi atom would *not* make an appreciable contribution to $\mathbf{B}_{SO}$. The

TABLE I. The values for the effective mass m^* (in free-electron mass), the coefficient α (in eVÅ), and the expectation value $\langle\mathbf{m}\rangle_\pm$ of the magnetization density (in Bohr magneton).

System	m^*	α	$\langle\mathbf{m}\rangle_\pm$
$[(ZnO)_{24}]_5$:Bi_{Zn}	0.36	0.080	$(\mp0.11, \pm0.46, \mp0.03)$
$[(ZnO)_{24}]_5 + Bi$:Bi_{Zn}	0.39	0.095	$(\pm0.04, \pm0.32, \pm0.34)$

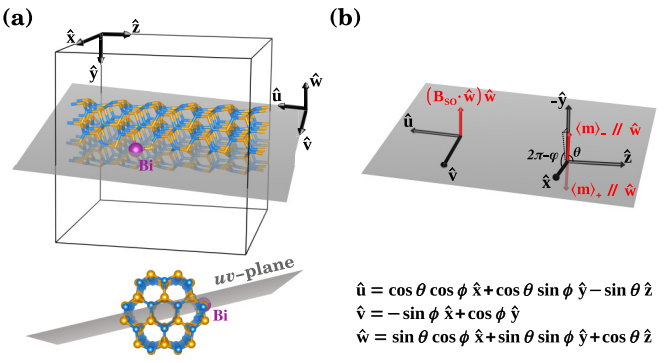

FIG. 2. (a) The uv plane that is perpendicular to $\langle\mathbf{m}\rangle_\pm$ and the uvw coordinate system are shown for $[(ZnO)_{24}]_5$:Bi_{Zn}. (b) A drawing showing the w component of $\mathbf{B}_{SO}$ in the direction parallel to $\langle\mathbf{m}\rangle_-$.

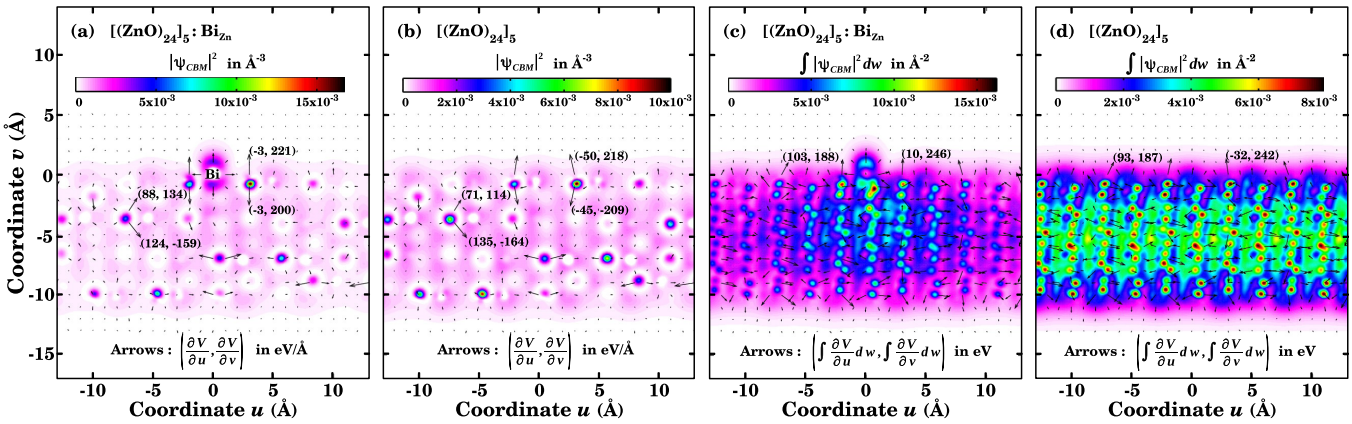

FIG. 3. The arrows represent (a, b) the potential gradient on the uv plane that is perpendicular to $\langle \mathbf{m} \rangle_{\pm}$ and (c, d) the vector quantity $(\int \frac{\partial V}{\partial u} dw, \int \frac{\partial V}{\partial v} dw)$ for (a, c) Bi-doped and (b, d) undoped ZnO nanowires. Colored contour plots of (a, b) the CBM state charge density $|\psi_{\mathrm{CBM}}|^2$ and (c, d) the integrated quantity $\int |\psi_{\mathrm{CBM}}|^2 dw$ are superimposed.

inhomogeneity of the potential gradient is further characterized in Figs. 3(c) and 3(d) with the aid of integrated quantities $(\int \frac{\partial V}{\partial u} dw, \int \frac{\partial V}{\partial v} dw)$ and $\int |\psi_{\mathrm{CBM}}|^2 dw$. A comparison of the arrows in Fig. 3(a) [Fig. 3(c)] with those in Fig. 3(b) [Fig. 3(d)] also indicates that the foregoing spatial inhomogeneity is *not* induced by the dopant. However, as will be elaborated in the Appendix, the incorporation of the dopant reduces the symmetry of the potential, rendering the CBM wave function to possess a lower symmetry. If the symmetry of the latter was conserved (i.e., remained the same as in the undoped ZnO nanowire), the matrix element $\langle \mathbf{B}_{\mathrm{SO}}(\mathbf{k}) \rangle$ in Eq. (2) would vanish, and no SO splitting could occur (which is clearly not the case). Nonetheless, the change in the potential gradient due to the dopant is small, as quantified in the Appendix. It can accordingly be said that the effective field $\mathbf{B}_{\mathrm{SO}}$ originates mostly from the nonvanishing potential gradient of the host (ZnO) nanowire, owing to its noncentrosymmetric (wurtzite) structure. In sum, on one hand the donation of electrons of the Bi dopant leads to magnetization of the CB states, and on the other hand, the inhomogeneity of the potential gradient of the host nanowire gives rise to an effective SO field $\mathbf{B}_{\mathrm{SO}}$. Considering a Zeeman-type interaction, according to Eq. (2), between $\mathbf{B}_{\mathrm{SO}}$ and the conduction electrons in the foregoing CB states explains the SO splitting of the bands shown in Figs. 1(c) and 1(d).

It is discernible in Figs. 3(a) and 3(c) that the CBM wave function is slightly localized in the regions close to the dopant, which has nevertheless comparable contributions from the dopant and host atoms. The latter precludes formation of a two-dimensional electron gas [although the lowest conduction bands in Fig. 1(c) are partially occupied], which means that the SO splitting in the Bi-doped ZnO nanowire does *not* originate from the Rashba interaction [27]. It should also be pointed out that the band splitting in Figs. 1(c) and 1(d) is *not* caused by the Dresselhaus effect [26] since the Dresselhaus spin splitting does *not* occur along the k_z direction in wurtzite semiconductors [41] such as ZnO [42].

In order to see *if* doping a ZnO nanowire with elements other than Bi causes a spin splitting along the momentum axis as in Fig. 1(c), we repeated geometry optimizations and electronic structure calculations by replacing Bi with Tl, Au, or Sb. Figures 4(a)–4(d) display the electronic energy bands calculated for $[(\mathrm{ZnO})_{24}]_5$:$\mathrm{Bi_{Zn}}$, $[(\mathrm{ZnO})_{24}]_5$:$\mathrm{Sb_{Zn}}$, $[(\mathrm{ZnO})_{24}]_5$:$\mathrm{Tl_{Zn}}$, and $[(\mathrm{ZnO})_{24}]_5$:$\mathrm{Au_{Zn}}$, respectively, which are colored to reflect the percent contribution from the dopant (Bi, Sb, Tl, or Au) to the electronic states. The coloring is accomplished by computing the contributions from the dopant and host (Zn and O) atoms that are obtained by projecting the state wave functions onto spherical harmonics within a sphere around each atom. We see that the SO splitting in $[(\mathrm{ZnO})_{24}]_5$:$\mathrm{Sb_{Zn}}$ is virtually negligible, which is as anticipated because the SO effects are much less pronounced for a lighter (Sb) atom compared to a heavier (Bi) atom. We find in fact that the value of α computed for $[(\mathrm{ZnO})_{24}]_5 : \mathrm{Sb_{Zn}}$ is *an order of magnitude* smaller than the respective value for $[(\mathrm{ZnO})_{24}]_5$:$\mathrm{Bi_{Zn}}$. On the other hand, doping with heavy elements Tl or Au results in a *nonzero* magnetic moment owing to formation of *gap states* with *flat* dispersion [cf. Figs. 4(c) and 4(d)]. Thus, the SO splitting of CBM in $[(\mathrm{ZnO})_{24}]_5 : \mathrm{Tl_{Zn}}$ and $[(\mathrm{ZnO})_{24}]_5 : \mathrm{Au_{Zn}}$ occurs along the energy (as opposed to momentum) axis.

Figures 5 and S2 (see Ref. [39]) show the variation of the linear coefficient α introduced in Eq. (1) with the Bi concentration for a set of host nanowires $[(\mathrm{ZnO})_N]_n$ with increasing thicknesses corresponding to $N = 24$, 54, and 96. For each value of N, a parametrization of α as a function of the supercell length L along the wire axis was performed, introducing two parameters A and λ, which is shown in the inset of Fig. 5. The latter is used to plot α versus the *number of Bi atoms per ZnO unit* (Fig. 5) and the Bi concentration in units of cm^{-1} [Fig. S2 (see Ref. [39])]. We see that α tends to reduce as the Bi concentration diminishes, which is in line with the fact that the linear-in-k splitting does *not* occur in the *absence* of the dopant. Furthermore, the thicker the host nanowire the smaller the α value in Fig. 5. It is thus clear that the value of α, which manifests the degree of linear-in-k splitting, could be tuned by adjusting the dopant concentration. The latter can be achieved by *either* decreasing the amount of the dopants (for a given ZnO nanowire) *or* increasing the number of Zn-O pairs, i.e., using a thicker nanowire. Consequently, doping-induced

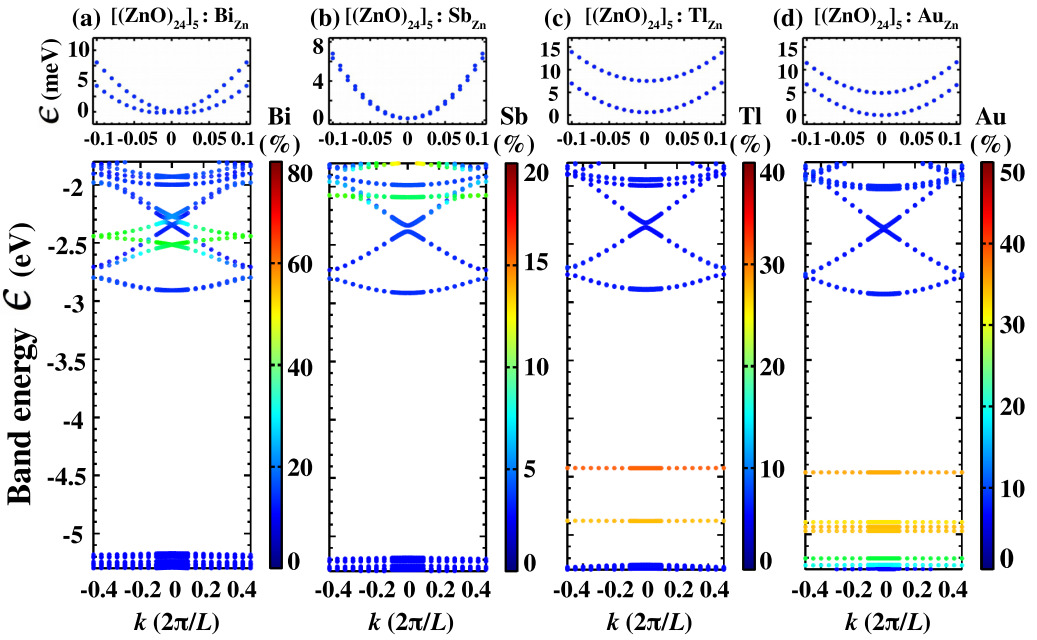

FIG. 4. The electronic energy bands calculated for (a) $[(ZnO)_{24}]_5$:Bi_{Zn}, (b) $[(ZnO)_{24}]_5$:Sb_{Zn}, (c) $[(ZnO)_{24}]_5$:Tl_{Zn}, and (d) $[(ZnO)_{24}]_5$:Au_{Zn}. The circles are colored to reflect the percent contribution from the dopant (Bi, Sb, Tl, or Au) to the electronic states. The upper panels show a closeup view of the *two* lowest conduction bands.

spin splitting in Bi-doped ZnO nanowires could be tuned and controlled by not only adjusting the amount of the dopants but also choosing a host nanowire of an adequate thickness.

Bismuth has a low solubility in zinc oxide, which is known to give rise to the Bi *segregation* observed in ZnO varistors [24,43]. In accordance with this, our theoretical characterization [22] of Bi-doped ZnO nanowires in a site-specific manner (as regards the location and charge state of the dopant) showed that the dopant (Bi) atoms are predominantly substituted into the Zn sites on the nanowire surface. This implies that the doping configuration displayed in Fig. 1(a) would abound in the defect structure of Bi-doped ZnO nanowires. Here we employ defect calculations to see *if* the configurations displayed in Figs. 1(a) and 1(b) could be *realized* by putting the host nanowire into contact with a reservoir of bismuth. Thus, the formation energy of the Bi dopant in these configurations is plotted as a function of the Bi chemical potential μ_{Bi} in Fig. 6(b) under Zn-*rich* as well as Zn-*poor* conditions. The formation of an adsorbed Bi atom, denoted as $[(ZnO)_{24}]_5 + Bi$, is also considered, for which the lowest-energy configuration is shown in Fig. 6(a). The values of μ_{Bi} corresponding to an equilibrium of the foregoing doping configurations with a reservoir consisting of (i) the Bi monomer gas, (ii) the Bi_2 dimer gas [44], (iii) the adsorbed Bi atoms, or (iv) the Bi solid are marked in Fig. 6(b). It is seen that the formation energies of $[(ZnO)_{24}]_5$:Bi_{Zn} and $[(ZnO)_{24}]_5 + Bi$:Bi_{Zn} are both *negative* under Zn-poor (i.e., O-rich) conditions, *regardless* of the bismuth reservoir. Hence these doping configurations can clearly be *realized* by putting the host nanowire into contact with an adequate reservoir of Bi under controlled thermodynamic conditions.

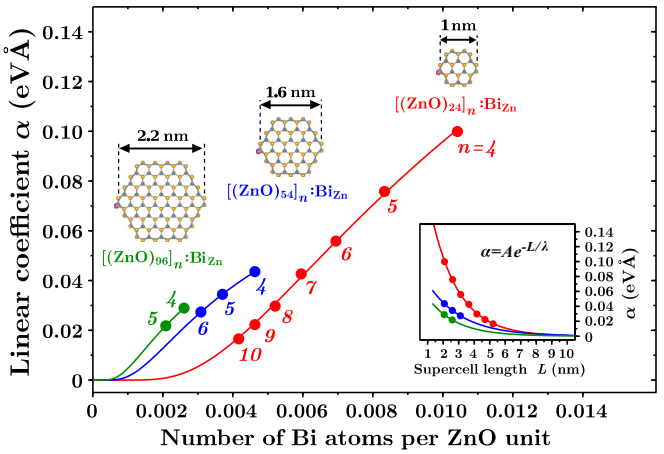

FIG. 5. The variation of the linear coefficient α introduced in Eq. (1) with the number of Bi atoms per ZnO unit and (inset) the supercell length L along the wire axis.

The *stability* of the foregoing doping configurations, cf. Figs. 1(a) and 1(b), is examined, in a *relative* manner, by performing *ab initio* MD simulations at temperature 600 K. The trajectories of atoms for $[(ZnO)_{24}]_5$:Bi_{Zn}, $[(ZnO)_{24}]_5$, and $[(ZnO)_{24}]_5 + Bi$:Bi_{Zn} attained from the position of atoms (averaged over every 100 MD steps) are displayed in Figs. 6(c), 6(e), and 6(g), respectively. The respective graphs of the temperature T (also averaged over every 100 MD steps) versus MD steps are given in Figs. 6(d), 6(f), and 6(h), which show that the temperature fluctuations are restricted to an interval of 20 K about the thermostat temperature $\bar{T} = 600$ K. The duration of our MD simulations is 5 ps (excluding the equilibration stage of 1 ps), which is likely shorter than needed for a complete prediction of the dynamical behavior of the studied systems. Nevertheless, it is clear from Figs. 6(c), 6(e), and 6(g) that

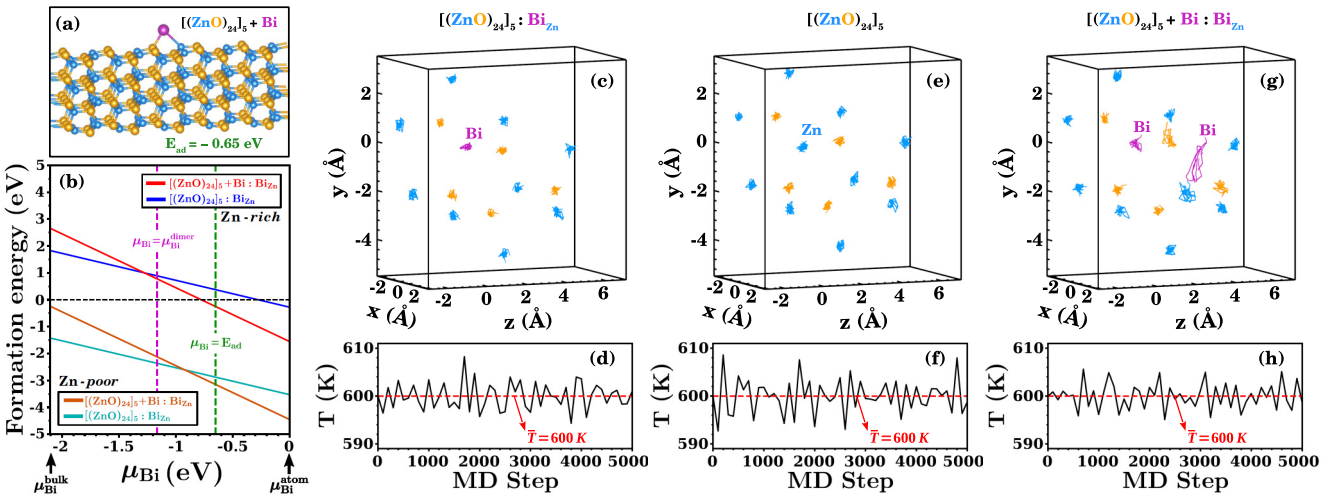

FIG. 6. (a) Optimized atomic structure for $[(ZnO)_{24}]_5 + Bi$. (b) The formation energies of $[(ZnO)_{24}]_5$:Bi_{Zn} and $[(ZnO)_{24}]_5 + Bi$:Bi_{Zn} as a function of the Bi chemical potential μ_{Bi} under Zn-*rich* and Zn-*poor* conditions; the zero of μ_{Bi} is set to E(Bi). (c, e, g) The trajectories of atoms for (c) $[(ZnO)_{24}]_5$:Bi_{Zn}, (e) $[(ZnO)_{24}]_5$, and (g) $[(ZnO)_{24}]_5 + Bi$:Bi_{Zn}, attained from the position of atoms averaged over every 100 MD steps, in the course of *ab initio* MD simulations; only *five* O and *ten* Zn atoms of the host nanowire are shown, which correspond to the first and second neighbors of the *two* Bi atoms in (g). (d, f, h) The respective graphs showing the temperature T (in black) vs MD steps, where the thermostat temperature $\bar{T}$ is marked in red.

not only the host (Zn, O) atoms but also the Bi dopant and adatom show a tendency to restore their equilibrium positions at a temperature (600 K) considerably higher than room temperature. Whereas the Bi adatom [Fig. 6(g)] has the *greatest* displacement, the Bi dopant [Fig. 6(c) and 6(g)] has the *least* displacement in comparison to the displacements of the host (Zn, O) atoms. This indicates that the Bi-doped ZnO nanowire is in fact *as stable as* the undoped ZnO nanowire, which is also supported by an overall comparison of the trajectory plots in Figs. 6(c) and 6(e). Furthermore, although our MD simulations were not intended to study the diffusion characteristics of Bi species on the surface of the ZnO nanowire, it is clear from Fig. 6(g) that the presence of the Bi adatom does *not* harm the stability of the *substitutional* Bi dopant.

IV. CONCLUSION

The present paper demonstrates that doping a semiconducting nanowire with a heavy element could be an effective means to lift Kramers degeneracy of the conduction-band states. In particular, doping ZnO nanowires with Bi is identified as a means to design quasi-one-dimensional materials for spintronic applications, thanks to the occurrence of the linear-in-k spin-orbit splitting explored in this paper. It is noteworthy that the degree of the linear-in-k spin splitting, which would facilitate the control of spin polarization of the conduction electrons in Bi-doped ZnO nanowires by applying external *electric* fields, could be tuned by adjusting the dopant concentration. Our findings suggest that Bi-doped ZnO nanowires, which are found to be stable under reasonable thermodynamic conditions, could be used in spintronic applications.

ACKNOWLEDGMENTS

The authors acknowledge financial support from the Scientific and Technological Research Council of Turkey (TUBITAK) through Grant No. 114F155. The numerical calculations reported here were carried out at the High Performance and Grid Computing Center (TRUBA Resources) of TUBITAK ULAKBIM.

APPENDIX: LOWERING OF THE SYMMETRY IN THE PRESENCE OF THE DOPANT

From the perspective of symmetry, the linear-in-k SO splitting in Eq. (1) *cannot* be attributed to the host (ZnO) nanowire. Since the irreducible representations of C_{6v} compatible with spin are doubly degenerate, *no* spin splitting occurs along the Γ-A direction of the wurtzite Brillouin zone [45]. This is also valid for the ZnO nanowires employed here, the point group of which is C_{6v}, in the absence of the Bi dopant [cf. Fig. S1(a) (see Ref. [39])]. It is thus clear that the SO splitting explored here occurs due to lowering of the symmetry in the presence of the dopant. Here we present an analysis of the latter in terms of doping-induced changes in the potential gradient and the CBM wave function since the expectation value of the SO interaction operator involves *both* [cf. Eq. (2)]. This analysis is conducted by plotting the yz planar average of the state charge density $\rho = |\psi_{\mathbf{k}}|^2$ in Fig. 7(a) and the potential gradient $\partial V/\partial x$ in Fig. 7(b) with respect to x, where $\mathbf{k}$ is set as the wave vector at which the CBM occurs. It is instructive to compare the Bi-doped nanowire to not only the undoped nanowire but also the Sb-doped nanowire because $[(ZnO)_N]_n$:Bi_{Zn} and $[(ZnO)_N]_n$:Sb_{Zn} possess the same symmetry. As respectively seen in Figs. 7(a) and 7(b), both $\langle\rho\rangle$ and $\langle\partial V/\partial x\rangle$ have asymmetric profiles in the presence of the dopant (Bi or Sb), which could be explained by noting that the reflection symmetry with the mirror plane at the center of the nanowire is lost when the dopant is incorporated. It is also seen that the doping-induced change in $\langle\partial V/\partial x\rangle$ is not noteworthy whereas the change in $\langle\rho\rangle$ shows a significantly asymmetric profile, as will be quantified in the next paragraph. Comparing the curves for $[(ZnO)_N]_n$:Bi_{Zn} and $[(ZnO)_N]_n$:Sb_{Zn} in Fig. 7(b) to each

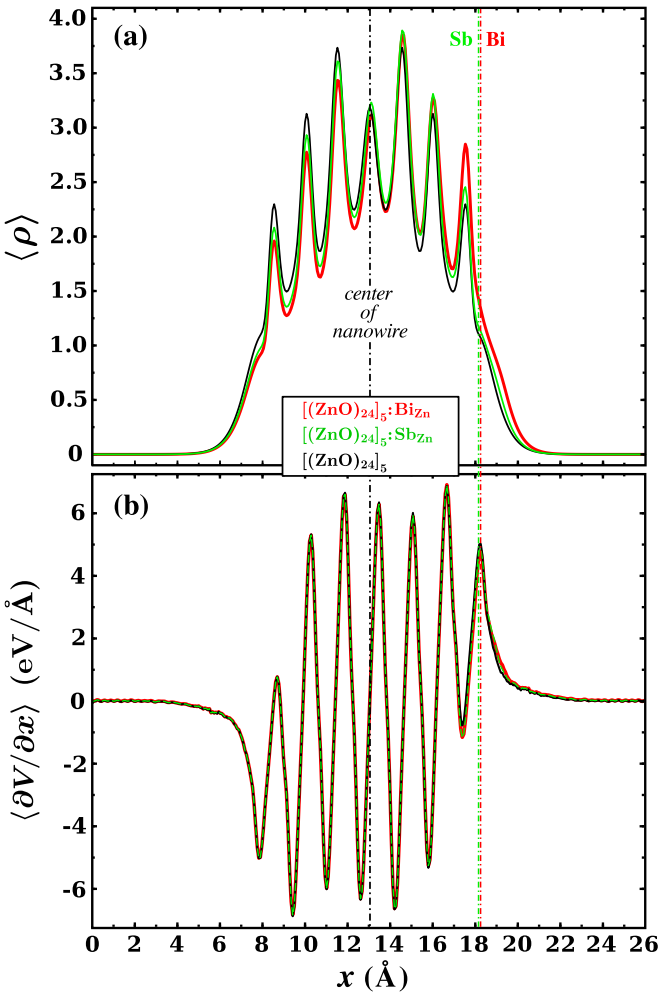

FIG. 7. The curves in red, green, and black represent the plots of the yz planar average of (a) the state charge density $\langle\rho\rangle$ and (b) the potential gradient $\langle\partial V/\partial x\rangle$ vs x, cf. Fig. 2, for $[(ZnO)_{24}]_5$:Bi_{Zn}, $[(ZnO)_{24}]_5$:Sb_{Zn}, and $[(ZnO)_{24}]_5$, respectively. The vertical dash-dotted lines mark the center of the nanowire (black) as well as the positions of Bi (red) and Sb (green) atoms on the x axis.

other, it is seen that the change in the potential gradient is quite indifferent to the type of dopant, which is seemingly not the case with the state charge density since the red curve, in comparison to the green curve, is in a larger deviation from the black (symmetric) curve in Fig. 7(a). These comparisons show that the essential difference between doping with Bi and Sb pertains mostly to the change in the CBM wave function, rather than the potential gradient. This means that reducing the symmetry of $\vec{\nabla}V$ would *not necessarily* produce a SO splitting as in Eq. (1); it *must* be accompanied by the adequate modification of the state wave function to a lower symmetry, cf. Fig. 7(a), as in the case of $[(ZnO)_N]_n$:Bi_{Zn}.

The lowering of the symmetry in the presence of the dopant (Bi or Sb) can be quantified by introducing the following quantities: $I = \int dx \langle\rho\rangle\langle\frac{\partial V}{\partial x}\rangle$, $I_0 = \int dx \langle\rho_0\rangle\langle\frac{\partial V_0}{\partial x}\rangle$, $I_V = \int dx \langle\rho\rangle\langle\frac{\partial \Delta V}{\partial x}\rangle$, and $I_\rho = \int dx \langle\Delta\rho\rangle\langle\frac{\partial V}{\partial x}\rangle$, where $\Delta V(\mathbf{r}) = V(\mathbf{r}) - V_0(\mathbf{r})$ and $\Delta\rho(\mathbf{r}) = \rho(\mathbf{r}) - \rho_0(\mathbf{r})$, and $\rho(\mathbf{r})$ and $V(\mathbf{r})$ [$\rho_0(\mathbf{r})$ and $V_0(\mathbf{r})$] denote the state charge density and potential of the doped [undoped] nanowire. Note the following:

(i) $I = I_0 + I_V + I_\rho$; the computed value of $I = 0.08$ eV for $[(ZnO)_{24}]_5$:Sb_{Zn} is *half* of that for $[(ZnO)_{24}]_5$:Bi_{Zn} for which $I = 0.16$ eV.

(ii) I_0 involves only the host-related quantities, and so $I_0 = 0$ owing to the symmetry of the undoped ZnO nanowire.

(iii) I_V and I_ρ are "measures" of the degree of doping-induced asymmetry due to the change in the potential and in the state charge density, respectively.

We obtain $I_V = -0.03$ eV for *both* $[(ZnO)_{24}]_5$:Bi_{Zn} and $[(ZnO)_{24}]_5$:Sb_{Zn} whereas $I_\rho = 0.19$ and 0.11 eV for $[(ZnO)_{24}]_5$:Bi_{Zn} and $[(ZnO)_{24}]_5$:Sb_{Zn}, respectively. Note that I_V takes the same value for both dopants, which is significantly smaller than the respective I_ρ values. This means that the doping-induced asymmetry due to the changes in the state wave function, rather than in the potential gradient, is pronounced. Accordingly, what really differentiates the cases of doping Bi versus Sb is the lowering of the symmetry of the CBM wave function.

[1] A. V. Moroz and C. H. W. Barnes, Phys. Rev. B **60**, 14272 (1999).
[2] S. Zhang, R. Liang, E. Zhang, L. Zhang, and Y. Liu, Phys. Rev. B **73**, 155316 (2006).
[3] S. Pramanik, S. Bandyopadhyay, and M. Cahay, Phys. Rev. B **76**, 155325 (2007).
[4] C. Quay, T. Hughes, J. Sulpizio, L. Pfeiffer, K. Baldwin, K. West, D. Goldhaber-Gordon, and R. De Picciotto, Nat. Phys. **6**, 336 (2010).
[5] J.-W. Luo, L. Zhang, and A. Zunger, Phys. Rev. B **84**, 121303 (2011).
[6] A. Crepaldi, G. Bihlmayer, K. Kern, and M. Grioni, New J. Phys. **15**, 105013 (2013).
[7] J. Park, S. W. Jung, M.-C. Jung, H. Yamane, N. Kosugi, and H. W. Yeom, Phys. Rev. Lett. **110**, 036801 (2013).
[8] C.-L. Hsu and S.-J. Chang, Small **10**, 4562 (2014).
[9] G. Li, A. Sundararajan, A. Mouti, Y.-J. Chang, A. R. Lupini, S. J. Pennycook, D. R. Strachan, and B. S. Guiton, Nanoscale **5**, 2259 (2013).
[10] M. J. Spencer, Prog. Mater. Sci. **57**, 437 (2012).
[11] O. Lupan, T. Pauport, T. Le Bahers, B. Viana, and I. Ciofini, Adv. Funct. Mater. **21**, 3564 (2011).
[12] M.-P. Lu, J. Song, M.-Y. Lu, M.-T. Chen, Y. Gao, L.-J. Chen, and Z. L. Wang, Nano Lett. **9**, 1223 (2009).
[13] G.-D. Yuan, W.-J. Zhang, J.-S. Jie, X. Fan, J.-X. Tang, I. Shafiq, Z.-Z. Ye, C.-S. Lee, and S.-T. Lee, Adv. Mater. **20**, 168 (2008).
[14] Y. Huang, Y. Zhang, Y. Gu, X. Bai, J. Qi, Q. Liao, and J. Liu, J. Phys. Chem. C **111**, 9039 (2007).
[15] Y. Q. Chang, D. B. Wang, X. H. Luo, X. Y. Xu, X. H. Chen, L. Li, C. P. Chen, R. M. Wang, J. Xu, and D. P. Yu, Appl. Phys. Lett. **83**, 4020 (2003).
[16] J. B. Cui and U. J. Gibson, Appl. Phys. Lett. **87**, 133108 (2005).

[17] J. Segura-Ruiz, G. Martínez-Criado, M. H. Chu, S. Geburt, and C. Ronning, Nano Lett. **11**, 5322 (2011).
[18] J. Iqbal, X. Liu, H. Zhu, C. Pan, Y. Zhang, D. Yu, and R. Yu, J. Appl. Phys. **106**, 083515 (2009).
[19] X. Ma, Thin Solid Films **520**, 5752 (2012).
[20] A. Hoffmann and S. D. Bader, Phys. Rev. Applied **4**, 047001 (2015).
[21] C. Xu, J. Chun, D. E. Kim, J.-J. Kim, B. Chon, and T. Joo, Appl. Phys. Lett. **90**, 083113 (2007).
[22] Ç. Kılıç, M. Aras, and S. Güler-Kılıç, in *Low-Dimensional and Nanostructured Materials and Devices: Properties, Synthesis, Characterization, Modelling and Applications*, edited by H. Ünlü, M. N. J. Horing, and J. Dabowski (Springer, New York, 2016), pp. 401–421.
[23] F. X. Xiu, L. J. Mandalapu, Z. Yang, J. L. Liu, G. F. Liu, and J. A. Yarmoff, Appl. Phys. Lett. **89**, 052103 (2006).
[24] A. Smith, J. Baumard, P. Abélard, and M. Denanot, J. Appl. Phys. **65**, 5119 (1989).
[25] R. H. Silsbee, J. Phys.: Condens. Matter **16**, R179 (2004).
[26] G. Dresselhaus, Phys. Rev. **100**, 580 (1955).
[27] Yu. A. Bychkov and É. I. Rashba, JETP Lett. **39**, 78 (1984).
[28] G. Kresse and J. Furthmüller, Phys. Rev. B **54**, 11169 (1996).
[29] S. L. Dudarev, G. A. Botton, S. Y. Savrasov, C. J. Humphreys, and A. P. Sutton, Phys. Rev. B **57**, 1505 (1998).
[30] J. P. Perdew, K. Burke, and M. Ernzerhof, Phys. Rev. Lett. **77**, 3865 (1996).
[31] P. E. Blöchl, Phys. Rev. B **50**, 17953 (1994).
[32] G. Kresse and D. Joubert, Phys. Rev. B **59**, 1758 (1999).
[33] M. Aras and Ç. Kılıç, J. Chem. Phys. **141**, 044106 (2014).
[34] D. Hobbs, G. Kresse, and J. Hafner, Phys. Rev. B **62**, 11556 (2000).
[35] M. Marsman and J. Hafner, Phys. Rev. B **66**, 224409 (2002).
[36] S. Nosé, J. Chem. Phys. **81**, 511 (1984).
[37] P. Tronc, V. Stevanovic, I. Milosevic, and M. Damnjanovic, Phys. Status Solidi B **243**, 1750 (2006).
[38] J. Nitta, T. Akazaki, H. Takayanagi, and T. Enoki, Phys. Rev. Lett. **78**, 1335 (1997).
[39] See Supplemental Material at http://link.aps.org/supplemental/10.1103/PhysRevB.95.155404 for Fig. S1, which displays the electronic energy bands calculated for $[(ZnO)_{24}]_5$, $[(ZnO)_{24}]_5$:Bi_{Zn}, $[(ZnO)_{24}]_5 + Bi$:Bi_{Zn}, and $[(ZnO)_{24}]_5 + Bi$, which are colored according to the contribution of atoms, and Fig. S2, which shows the plot of the linear coefficient α versus the Bi concentration in units of cm^{-1}.
[40] A. Davydov, *Quantum Mechanics*, 1st ed. (Pergamon, New York, 1965), p. 252.
[41] A. De and C. E. Pryor, Phys. Rev. B **81**, 155210 (2010).
[42] A. Schleife, F. Fuchs, C. Rödl, J. Furthmüller, and F. Bechstedt, Phys. Status Solidi B **246**, 2150 (2009).
[43] K.-I. Kobayashi, O. Wada, M. Kobayashi, and Y. Takada, J. Am. Ceram. Soc. **81**, 2071 (1998).
[44] A. Zajaczkowski, J. Czernecki, and A. Surulo, Calphad **52**, 66 (2016).
[45] L. C. Lew Yan Voon, M. Willatzen, M. Cardona, and N. E. Christensen, Phys. Rev. B **53**, 10703 (1996).